

- ① The Oort constants reveal the rotational features of the Milky Way disk in the solar neighborhood. The orbital properties of the Sun can be estimated from the Oort constants.
- ② and to understand the general kinematic properties of the MW disk.
- ③ Combining test particle simulations and the recent Gaia DR2 data, we

DRAFT VERSION APRIL 24, 2021

Typeset using L^AT_EX modern style in AASTeX63

- ④ From the simulation, it seems that it is necessary to limit the distance within 2 kpc, and latitude range $|b| < 20^\circ$ to achieve a good fit based on the longitudinal profiles of M_0 and V_{los} . Revisit the Oort constants measurement from Gaia DR2 observations generally not as good as the other kinematic tracers. However, reasonable Oort constants could be estimated if the latitude range is limited to $3^\circ < |b| < 15^\circ$

SHUFAN XIA,¹ KAREN MASTERS,¹ AND ZHAO-YU LI²
¹Haverford College, Department of Physics and Astronomy
²Shanghai Jiaotong University, Department of Astronomy

ABSTRACT

- ① The Oort constants parameterize stellar motion in the Milky Way Galaxy (MW). They describe the epicycle motions in radial, longitudinal, and latitude directions near the Sun. They prove Milky Way differential rotation and a flat MW rotation curve. An accurate determination of this set of constants helps us derive the MW rotation curve in the Sun's immediate neighborhood. ② They can be used to find local Galactic parameters, such as orbit ellipticity, solar distance from the Galaxy's center, etc. Gaia provides massive and exquisite data on parallax and proper motion of stars in the Milky Way. These data make it possible to determine the Oort constants in the solar vicinity with unprecedented accuracy. ③ This work re-examines the influence of different sampling criteria on the stellar distance and latitude ranges in the Galactic coordinate used to derive the Oort constants based on Gaia DR2 data. ④ We apply proper motion and line-of-sight velocity data from Gaia DR2 and compare the result with an idealized test particle simulation under an axisymmetric potential to determine the best stellar subsets for calculating the Oort constants. We found $A = , B = , C = , K =$ from Gaia DR2 observational data, while $A = , B = , C = , K =$ from our simulation. consistent with previous works.

1. INTRODUCTION

The simplest model of the Milky Way (MW) proposes that our galaxy is a flat circular disk, and stars move on perfectly circular orbits around the galactic center (GC). However, the structure and the dynamics of our galaxy are much more complicated. Our galaxy is a barred-spiral galaxy with non-axisymmetric and time-dependent perturbation to its potential. Due to perturbation in the MW potential, all stars have non-circular components to their orbital energy, so they move in elliptic and non-closed orbits (Binney & Merrifield 1998; Bovy 2017). The rotational kinematics of the MW are, therefore, complicated to quantify. The Oort constants are a set of

Corresponding author: Shufan Xia

sxia1@haverford.edu

⑤ with the criteria determined from our test particle simulations.

empirically derived kinematic parameters notated typically with A , B , C , and K that characterizes the local rotation properties in the Milky Way. They have been used extensively in the study of the rotational kinematics of our galaxy.

To help us keep track of the different velocities in the following discussion, here I list the notation for velocity components used throughout this paper. In Galactocentric cylindrical coordinate, v_{circ} or v_ϕ is the circular velocity about the Galactic Center(GC); v_r is the radial velocity with respect to the GC; v_z is vertical velocity away from the Milky Way (MW) plane. In Galactic coordinates (discussed further in Section 1.2), v_{los} is the line of sight velocity as seen from the Sun; v_l is the velocity component perpendicular to the line of sight in the longitude (l) direction; and v_b represents the velocity component perpendicular to the line of sight in the latitude (b) direction.

1.1. The Milky Way Rotation Curve

The rotation curves of galaxies are used to illustrate dependency of circular rotational velocity, v_ϕ , about the galactic center on distance from the center. Pioneered by Vera Rubin, galactic rotation curves have been studied as the evidence of Dark Matters. For our Milky Way, this rotation curve is flat but slightly declining from the radius of the Sun and beyond. The mass components and their distributions in our Galaxy have been derived from this curve. Fig. 1 shows a recent measurement of the MW rotation curve (Eilers et al. 2019). The overall rotation curve comes from adding up the contributions from different components of mass - the central bulge, stellar disc, other stellar components and the dark matter halo (Olling & Merrifield 1998).

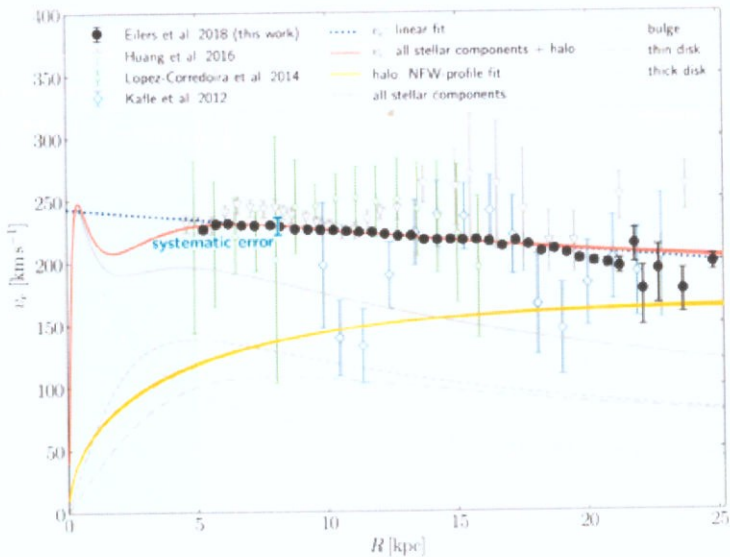


Figure 1: Recent measurements of the circular velocity curve of the Milky Way. The red curve is an approximate overall rotation curve (Eilers et al. 2019).

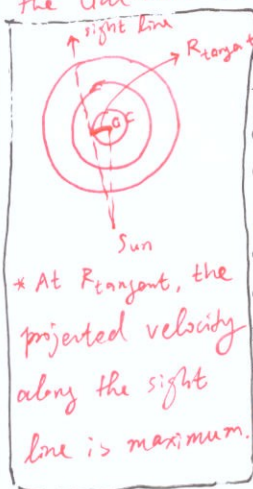
Using Newtonian Mechanics, we can connect velocity, potential, and mass distribution (Binney & Merrifield 1998); therefore, stellar kinematics is a mass probe. The application of measuring rotation curves are multiple: they can be used to study kinematics, evolutionary histories of galaxies, and departures from Keplerian form due to dark matter (Sofue & Rubin 2001). However, measuring the Milky Way rotation curve is challenging because of the observation constraints caused by our location in the Milky Way. We are in one of the spiral arms of the Galaxy, the Orion Arm (Binney & Merrifield 1998). This means that our line of sight is blocked by the dust in this spiral arm, so we can not observe stars on the other side of the Milky Way bulge. The fact that we are co-moving with the Galaxy also makes it challenging to determine the relative motion. (I am not sure if this is right and enough.) Therefore, measuring the whole rotation curve remains a challenging task.

Various tracers and methods have been used to track the rotation curve. Determining distances is always difficult for astronomers because the extinction from interstellar medium adds challenge to accurate measurement. For the inner region within the Sun, the MW rotation curve has been determined via the tangent-point method which uses the line of sight velocity measured observational from the shifts in the emission lines of the gas clouds in CO, H I, and H II regions under Doppler's effect (Levine et al. 2008). (I am not sure if this is right) Based on geometric and trigonometric derivations, this method is able determine distances and rotation velocity just from the radial velocities of gas clouds in a fixed direction but at different distances with respect to the observer. The rotation curve of the outer region beyond the Sun has been measured by other tracers, such as classical Cepheid (Joy 1939; Metzger et al. 1998; Mróz et al. 2019), RR Lyrae stars (Wegg et al. 2019), and luminous red giant stars (Eilers et al. 2019). Both classical Cepheids and RR lyrae stars are better for determining rotation curve because they are intrinsically bright and their distance-period relationship makes distance measurement more reliable. (Metzger et al. 1998).

The maximum line of sight velocity corresponds to the radius of the tangent point of the sight line relative to the Galactic center.

1.2. Oort constants

While many methods to obtain constraint on the rotation curve require difficult observational measurements across a very large space, we can use the Oort constants to describe local rotational properties. The Oort constants A and B (which are explained more in section 1.3 below) tell us the local rotational velocity around the Galactic Center and the local slope of the rotational curve (Binney & Merrifield 1998). The power of the Oort constants is that they are local parameters, but it enables us to test against different rotational models from their predicted rotation curves. This work looks at the Oort constants in the vicinity of our Sun. An accurate measurement of the Oort constants in this region will potentially help us determine the local rotation curve, Galactic radius, and rotational velocity of the Sun (Olling & Merrifield 1998), as well as the eccentricity of the solar orbit (Kuijken & Tremaine 1994; Metzger et al. 1998).



for the possible existence of the disk far from the S

constants

To study the local rotation near the Sun and the Oort requires an understanding of Galactic coordinates. They are in a spherical coordinate system, with the Sun at its center and its plane parallel to the Milky Way midplane. Galactic longitude l is the counter-clockwise azimuthal angle measured from the Galactic center at $l = 0$, and the Galactic longitude, b , is the elevation angle (See Fig.2). However, because the Sun has complicated non-circular velocity components, using the Sun as our reference frame is not very convenient. Instead, we ~~define~~^{adopt} a reference frame called the Local Standard Rest (LSR) as the origin in the Galactic coordinate system. LSR is located at the same position of the Sun, and following a perfect circular orbit around the GC at $v_\phi = 220 \text{ or } 224?$ km/s. Solar motion relative to the LSR is defined as ~~the~~^{the} peculiar motion (Binney & Merrifield 1998).

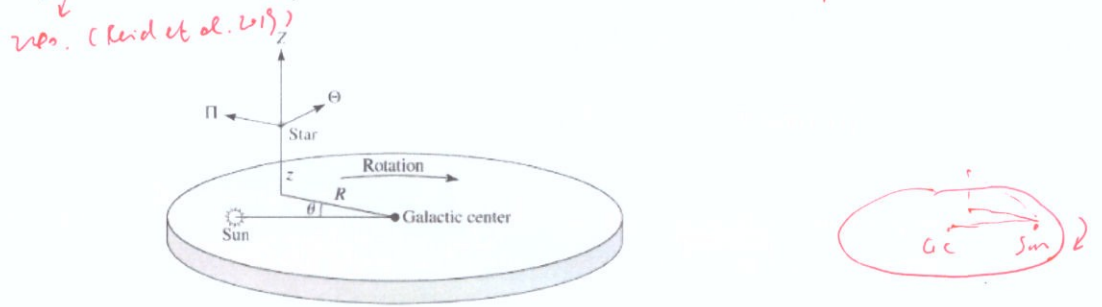


Figure 2: Galactic coordinate system. Figure adapted from Miros unknown year.

Use the figure in Binney & Tremaine (2018)

Assuming the Milky Way has axisymmetric potential and stars are on circular orbits, Oort (1927) derived Oort constants A and B via radial velocities and tangential proper motions as a function of Galactic longitude l by Taylor-expanding the local velocity field to the first order about the local rotational center. It is shown that the radial velocity and tangential velocity are proportional to $\cos 2l, \sin 2l$:

$$v_r = Ad \sin 2l \quad \text{and} \quad v_\perp = d(A \cos 2l + B) \quad (1)$$

$$\text{, where } A = -\frac{1}{2}\left(\frac{dv_{circ}}{dR} - \frac{v_{circ}}{R}\right)\Big|_{R_\odot} \text{ and } B = -\frac{1}{2}\left(\frac{dv_{circ}}{dR} + \frac{v_{circ}}{R}\right)\Big|_{R_\odot}.$$

In Oort's original measurement, he determined that near the Sun $A \approx 19$ (km/s/kpc) and $B \approx 24$ (km/s/kpc) (Oort 1927). The value, A describes the local shearing, and B describes local vorticity. The result of a non-zero A suggests that stars near the Sun have varying rotation angular velocity, providing the first strong evidence that the Milky Way is rotating differentially. This result supported an earlier rotation model of the MW hypothesized by Lindblad. In Lindblad's hypothesis that the Galactic systems may be divided into subsystems (globular clusters). Each subsystem rotates around the Galactic center, and within each subsystem, objects rotate around a common axis but at different rotational speeds (Oort 1927). (Karen suggests deleting this chunk) (agreed)

The Oort constants were generalized to consider the Sun's peculiar motion with respect to nearby stars. It is derived analytically that the double sine (or cosine)

trend is distinguishable from the pattern due to the Sun's peculiar motion about nearby stars. Two additional constants were introduced to the function of radial and tangential velocity against l , namely C , and K (Ogrodnikoff 1932). These four constants, A , B , C , and K describe the transverse shear, vorticity, radial shear, and divergence in the local velocity field from Galactic rotation accordingly. The radial velocity (v_{los}) is:

$$v_{los} = d(K + C \cos 2l + A \sin 2l) \quad (2)$$

The proper motion in longitude and latitude direction, μ_l and μ_b , have the following dependence on $2l$ (Olling & Dehnen 2003):

$$\mu_l = (A \cos 2l - C \sin 2l + B) \cos b + \varpi(u_0 - v_0 \cos l) \quad (3)$$

$$\mu_b = -(A \sin 2l + C \cos 2l + K) \sin b \cos b + \varpi[(u_0 \cos l + v_0 \sin l) \sin b - w_0 \cos b] \quad (4)$$

In equations above, the single sin and cos terms represent the effect due to the Sun's peculiar motion (u_0, v_0, w_0).

The local slope of the rotation frequency (Ω) at the solar radius, $\frac{d\Omega}{dr}|_{R_\odot}$ is $-(A+B)$. If the Galaxy is not axi-symmetric, C and K are nonzero (Binney & Merrifield 1998, Ogrodnikoff 1932). In the Method section below, I will present the full derivation of Oort constants. The Fourier series approximation approach has also been used to derive Oort constants. Fourier coefficients of the $n = 0$ and $n = 2$ modes correspond to Oort Constants (Lin et al. 1978).

It must be emphasized that Oort constants can be extended to a set of functions depending on the distances from the Galactic center as we apply Taylor expansion velocity fields about different locations in the MW. Typically, the Oort functions vary at a rate of a few km/s/kpc per kpc (Olling & Merrifield 1998). For distant stars in the disk, a higher order of the streaming velocity field equation must be taken into consideration (Siebert et al. 2011). The Oort constants in the first order of the streaming velocity field equation are restrained to the rotation in the solar vicinity because the higher-order contributions will become significant at large distances (Bovy 2017). Due to the contribution from interstellar gas in the MW which density varied non-monotonically with distance from the Galactic center, between $0.9R_\odot$ and $1.2R_\odot$, the Oort functions $A(R)$ and $B(R)$ differ significantly from the general angular frequency dependence (Olling & Merrifield 1998). This suggests that when measuring the Oort constants, it is crucial to constrain the range of Galactic distance.

1.3. Measuring Oort constants

In order to measure the Oort constants based on Eq.?? and Eq.4, we need to have locations and velocities of stars in Galactic coordinates. From our vantage point on Earth, we can get radial velocities from the Doppler shift, and proper motions are measured optically by tracing the stars moving across the plane of the sky. Positions, radial velocities, and proper motions are then converted to the Galactic coordinate.

functions to
measure the

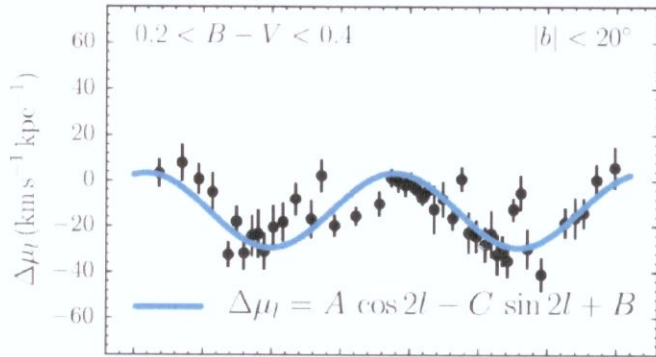


Figure 3: One example of historical measurement of Oort constants from Bovy (2017) with observed proper motion in Galactic longitude: the value on y -axis is corrected for the solar motion based on Eq.3. The averages $\mu_l(l)$ binned by l and their errors are plotted.

Many investigations have been conducted to attempt to use proper motion to determine the character of the non-uniformity of rotation and to measure the Oort constants. Fig.3 shows one example of measurement of Oort constants with proper motion from Bovy (2017). However, not all the results are in agreement (Kerr & Lynden-Bell 1986), which is mainly due to the absence of a complete proper motions catalog. A complete measurement of proper motion can give us stars distant enough that their individual random motions do not dominate their proper motions. It will also ensure sufficient sky coverage to allow the separation between the double sine curve of Galactic proper motions from the single sine curve due to the solar motion in Eq. ?? (Kerr & Lynden-Bell 1986). Although the observational precisions have been continuously developed, the values of A and B are still consistent with the values within the uncertainties. However, for the values of C and K , it is another story (Li et al. 2019). Besides needing a complete proper motion catalog, three other factors complicate an accurate determination of values for the Oort constants.

First, the effect of non-axisymmetric potential associated with spiral or bar structure is not taken into account in Oort's analysis. Observation data suggests the necessity of looking at a non-axisymmetric mode (Metzger et al. 1998). From the radial velocity of Cepheids, a significant zero-point offset (the Oort constant, K) in the radial velocities is suggested for a non-axisymmetric model. Metzger et al. (1998) also found a positive antisymmetric ellipticity component at R0. The deviations from the general axisymmetric velocity field, or the deviation from the Oort constants model specified by Eq 2, 3 and 4, could be used to study the non-circular motions in great detail and infer the mass associated with the spiral arms (Olling & Merrifield 1998).

Second, it is found that moderate strength in the spiral structure causes errors of order 5 km/s/kpc in A and B (Minchev & Quillen 2007). The spiral structure can be understood as waves where the spirals have concentrated stars. The streaming

motion caused by density waves depending on the local spiral structure is difficult to determine (Lin et al. 1978). Further, the spiral structure raises the level of random motions in the Galactic disk (Sellwood & Carlberg 2014). Determination of other structural parameters to account for the effects from the Milky Way spirals must be made after a basic circular model in Section 1.2.

Third, the nonuniform distribution of stars with measured parallax over longitude in conjunction with the solar peculiar motion contributes to significant $n = 0$ and $n = 2$ modes deviated from the first order Oort analysis using Fourier series approximation (Olling & Dehnen 2003). The nonuniform distribution of stars across l may be due to intrinsic density nonuniformity or observational errors due to interstellar extinction. This systematic error has a contribution to the longitudinal proper motion $\mu_l(l)$ indistinguishable from the effect of double \sin and \cos dependency. Olling & Dehnen (2003) suggested using the latitudinal proper motions $\mu_l(l)$ of stars at low latitudes could correct for the errors from mode mixing in Fourier approximation.

Recent progress

1.4. *Oort constants measurements based on Gaia data*

In previous decades, the HIPPARCOS telescope had been used extensively in studying the MW kinematics, including deriving local Oort Constants and the rotation curve from classical cepheid (Feast & Whitelock 1997, Mignard 2000, Olling & Dehnen 2003). The *Gaia* mission (Gaia Collaboration et al. 2016a), since its launch by the European Space Agency in 2013, has collected astrometric parameters with unprecedented accuracy and multitude, aiming to build a three-dimensional map of our Galaxy. By the second release of *Gaia* data, we have the parallax and proper motions of over 1.6 billion stars (Gaia Collaboration et al. 2018). This also includes stars in higher latitude with significant latitudinal proper motion. Therefore, *Gaia*'s large set of astrometric measurements allows the first truly local precise measurement of the Oort constants and investigation of fine local kinematic features.

Two studies using *Gaia* DR1 and DR2 to calculate the Oorts Constant in solar vicinity yielded results in agreement (Bovy 2017; Li et al. 2019). The current values of the Oort constants based on DR2 are $A = 15.1 \pm 0.1$, $B = -13.4 \pm 0.1$, $C = -2.7 \pm 0.1$, $K = -1.7 \pm 0.2$, all in the unit of km/s/kpc (Li et al. 2019). The slope of the rotation curve is determined from $-(A + B)$ which is negative, thus confirming a slightly declining rotational curve in the solar vicinity. And significant non-zero C and K further indicate non-axisymmetric potential (Bovy 2017; Li et al. 2019). This suggests applying the axis-symmetric assumption of Oort analysis should be carefully examined. Both studies found the local Oort constants varied among different stellar populations based on their positions in the Hertzsprung-Russell Diagram (i.e. stellar age). The result in Li et al. (2019) shows that the red giants deviate from the main-sequence stars in all four constants because they show more elliptical orbits and larger velocity dispersion. This finding is inconsistent with the suggestion in Olling & Dehnen (2003) that red giants are the “true” tracer of the Oort constants because

$B, C, K < 0$

they are old enough to be in equilibrium and distant enough to be unaffected by possible local anomalies. This disagreement suggests establishing an appropriate set of stars is critical to determine Oort constants accurately.

Previous work using HIPPARCOS and *Gaia* data to fit Oort constants used average proper motion binned by l , but fine features from each sample point in proper motion are neglected, for example, Fig.3 (Bovy 2017, Li et al. 2019). I will have to change this based on our discussion from Thursday. Neither work used radial velocity information to determine the local Oort constants because the radial velocity measurement is only available for a fraction of the stars in the *Gaia* data. However, a closer look at the radial velocity results and their deviation from the predicted theoretical model potentially entails significant information.

Revised Motivation of the research

1.5. Proposed research

Our work focus on the Main Sequence (and Red Giant stars) from *Gaia* DR2. We use their latitudinal and longitudinal proper motions, as well as their radial velocity to determine the local Oort constants in Solar vicinity.

In order to measure Oort constants to higher precision and to understand the influence of sample selection on the final results, this work examines the conventional constraints on data sampling. In previous measurements of Oort constants (Olling & Dehnen 2003; Bovy 2017; Li et al. 2019), the sampling limit on parallax and latitude were explained qualitatively without justification. For example, Olling & Dehnen (2003) suggested using the μ_b of low latitudes stars, while both Bovy (2017) and Li et al. (2019) adopted the $40^\circ < |b| < 50^\circ$ sampling criteria. Therefore, it is not clear, especially in the case of analyzing μ_b , which subsets of stars in observation data should be used to derive the Oort constants and how using different subsets affects the final results.

We also use a simple 3D toy model of simulated test particle under the near circular orbital motion assumption to obtain a theoretical prediction of longitudinal and latitudinal proper motion, μ_l and μ_b , and radial velocity v_{los} as functions of Galactic longitude l . The simulation samples 500,000 test particles moving under the MW potential specified by Bovy (2015). The goal of this model simulation and comparing it to observational data is twofold. First, it allows us to find the range of parallax and Galactic latitude that give the best stellar subset(s) for Oort constants measurement. Second, it helps us to characterize the deviations in *Gaia*'s observational result from the expected model. The larger significance of this work is to provide a sample selection guidance for future Oort constants analysis.

In addition, to derive the Oort constants and their uncertainties, this work applied the Monte Carlo Markov Chain(MCMC) method to fit both observational results from *Gaia* and the simulation results of the toy model to Eq. 2, 3 and 4. Detail of the sample selection, MCMC fitting, and simulation are included in the following

* 所有段首缩进不一致, auto indentation?

Eqs. 2, 3 and 4

Eq. 2

sections. In the result section, we explore the connection between our simulation and DR2 observational data together have not done it at all.

Finally, the recent third release of *Gaia* in December 2020 adds 200 million new samples to our database (?) We hope the result of this work will give some guidance and insights into deriving the Oort constants from this more complete catalogue in the near future.

2. METHODS

2.1. Derivation of The Oort constants

The Oort constants describe stellar streaming motions about the Sun in the Galactic coordinate, a right-handed coordinate where the direction from the Sun to the Milky Way (MW) galactic center is longitude $l = 0$ and positive x (Fig 2). Consider a flat 2D Galactic disk under axisymmetric potential and the cold limit in which all stars move on closed orbits e.g. as defined in Olling & Dehnen (2003). The position of a star on the disk is (x, y) , where $(0, 0)$ is at the Sun in the Galactic coordinate. The velocity field $\langle v \rangle$ gives the average velocity at each point on the disk. In solar vicinity, the velocity at (x, y) may be expanded in a Taylor series about the Sun: *Assuming the Sun is in a pure circular orbit,*

$$\langle v \rangle|_{(x,y)} = \underbrace{\langle v \rangle|_{(0,0)}}_{\text{LSR velocity}} + \begin{pmatrix} v_{xx}, v_{xy} \\ v_{yx}, v_{yy} \end{pmatrix} \Bigg|_{(0,0)} \begin{pmatrix} x \\ y \end{pmatrix} \quad (5)$$

$$= \langle v \rangle|_{(0,0)} + \begin{pmatrix} K + C, A - B \\ A + B, K - C \end{pmatrix} \Bigg|_{(0,0)} \begin{pmatrix} x \\ y \end{pmatrix}, \quad (6)$$

where A , B , C and K are the Oort constants. The relative velocity of the star as observed from the Sun is given by

$$\delta \langle v \rangle|_{(x,y)} = \langle v \rangle|_{(x,y)} - \langle v \rangle|_{(0,0)}. \quad (7)$$

The line of sight velocity is the component of $\delta \langle v \rangle$ parallel to the galactic distance d :

$$v_{los} = \hat{d} \cdot \delta \langle v \rangle = \frac{(x, y)}{d} \cdot \begin{pmatrix} K + C, A - B \\ A + B, K - C \end{pmatrix} \Bigg|_{(0,0)} \begin{pmatrix} x \\ y \end{pmatrix}. \quad (8)$$

After taking the dot product and applying trigonometric relations, we have

$$v_{los} = d[K + A \sin(2l) + C \cos(2l)] \quad (9)$$

Similarly, the longitudinal proper motion, perpendicular component of the relative velocity over d , is:

$$\mu_{\perp} = \frac{1}{d}(\hat{d} \times \delta \langle v \rangle) = B + A \cos(2l) - C \sin(2l) \quad (10)$$

In the model of local rotation and Galactic coordinates, because the Sun moves in a non-circular orbit about the GC which makes calculation unnecessarily complicated,

~~we define a hypothetical reference point, Local Standard of Rest (LSR), as the reference frame in Galactic coordinates. The LSR is at the same position of the Sun and moves on a circular orbit at 220 km s^{-1} , and the relative motions of the Sun with respect to this LSR is described by peculiar motion, (u_0, v_0, w_0) , velocity in radial, tangential and vertical direction respectively. I talked about LSR in the intro, should I combine them in intro? or keep both of them? After correcting the solar peculiar motion, Eq 9 and 10 turn to:~~

(combine them in intro, and mention here that the previous equations are based on the LSR.)

$$v_{los} = d[K + A \sin(2l) + C \cos(2l)] - u_0 \cos(l) - v_0 \sin(l) \quad (11)$$

$$\mu_l = B + A \cos(2l) - C \sin(2l) + \frac{1}{d}[u_0 \sin(l) - v_0 \cos(l)], \quad (12)$$

where the $\cos b$ term in Eq 12 accounts for the projection of distance onto the Galactic plane in a 3D MW disk. If the vertical velocity v_z of the star is non-zero, the latitudinal relative velocity at (l, b, d) is given by $v_z(\cos b) - v_r \sin(b)$ (Olling & Dehnen 2003), and the latitudinal proper motion is:

v_b ?

$$\mu_b = -(A \sin 2l + C \cos 2l + K) \sin b \cos b + \varpi[(u_0 \cos l + v_0 \sin l) \sin b - w_0 \cos b]. \quad (13)$$

Eq 11, 12 and 13 together give a model to determine Oort constants from observational data, and the full model parameter is $\theta(A, B, C, K, u_0, v_0, w_0)$. probably will delete this sentence after I confirm we are using the value (u_0, v_0, w_0) from Schonrich 2012 for solar peculiar motion.

Karen suggests explaining parallax and error in observation.

2.2. The Gaia Sample selection and stellar parameter estimation

The Gaia (Global Astrometric Interferometer for Astrophysics) mission of the European Space Agency (ESA) surveys about one billion stars in the MW photometrically and spectroscopically to make the most accurate three-dimensional map of the Galaxy. Gaia samples kinematic tracers to a magnitude limit of at least $G = 20$ mag in the MW disks, bulge, and halo. The instrument package of Gaia spacecraft comprises two identical optical telescopes/imaging systems, a radial velocity spectrometer, and blue and red photometers. The unfiltered, white-light photometric G band of the optical telescope covers 330–1050 nm (Gaia Collaboration et al. 2016). The parallax uncertainties are 0.5 mas at $G = 20$. The uncertainties in proper motion are 0.5 mas yr⁻¹ at $G = 20$ (Gaia Collaboration et al. 2018).

The radial-velocity spectrometer obtains radial velocities by measuring the Doppler-shift in the lines of stellar spectra. DR2 has the radial velocity of more than 7.2 million stars with a mean $G = 4 – 13$ mag and an effective temperature in the range 3550 to 6900 K. The overall precision of the radial velocities range from 200–300 m s⁻¹ to 1.2–3.5 km s⁻¹ (Gaia Collaboration et al. 2016).

Astrophysical parameters such as effective temperature, surface gravity, metallicity of the stars, and extinction are derived from the BP and RP data measured by the

blue and red photometers over the wavelength ranges 330–680 nm and 630–1050 nm (Gaia Collaboration et al. 2016).

In December 2020, ESA released the third intermediate *Gaia* data (EDR3). This version of release catalogs the positions and proper motions, and other photometric data of 1,811,709,771 stars, 1,692,919,135 entries of which are updated from DR2. The radial velocity data in EDR3 is added from the 7.2 million data in DR2 after deleting 4000 wrong entries. Furthermore, EDR3 deleted several entries from DR2, including color excess, extinction, and tag for marking variable star samples (Gaia Collaboration et al. 2020). I used the TAP service from TOPCAT (Tool for Operations on Catalogues And Tables) to access, process, and select the DR2 and EDR3 data (Taylor 2005).

Since the first-order Taylor approximation in Eq 6 is only appropriate for Solar vicinity, the stellar samples are limited to the region within 500 pc (2mas) from the Sun. And restricting parallax/error ≥ 10 will avoid additional bias from inverting the parallax to estimate distance (Luri et al. 2018). The uncertainties in the BP and RP fluxes are restrained to less than 10% in making the Hertzsprung–Russell (H-R) diagram and selecting the main sequence samples. Potential duplicate sources are also removed.

The main sequence stars are selected by drawing on the H-R diagram in TOPCAT. Extinction A_G and color excess $E(B-V)$ must be considered when making an H-R diagram to reflect the properties of stars accurately. However, spectroscopic data, such as radial velocity, extinction, and color excess are not yet available for the 100 million newly added stars in EDR3. These data are expected to be published in DR3 in the first half of 2022 (Gaia Collaboration et al. 2020). Instead of doing a cross-match with DR2 samples, $E(B-V)$ in EDR3 are calculated from the DUSTMAP python library because the new spectroscopic measurements in EDR3 and DR3 use different blue and red photometers than those in DR2. DUSTMAP gives a 3D map of interstellar dust reddening probabilistically based on broadband photometric measurement from Pan-STARRS 1, 2MASS, and Gaia parallaxes (Green 2018). Each (l, b, d) corresponds to a color excess value in the default *bayestar17* module in DUSTMAP, which I multiplied with $R_v = 3.1$ to get the extinction. For EDR3, the position data is first retrieved from TOPCAT, then used to find $E(B-V)$ and A_G in python. The original data along with calculated $E(B-V)$ and A_G are used to plot H-R in TOPCAT again, and I drew out the main sequence samples on this diagram. Fig 4 shows the H-R diagram and Main sequence star samples in DR2 and EDR3 after applying parallax, extinction and color excess corrections. For DR2, color excess and extinction values used are from Gaia observation.

Because the local Oort constants varied among different stellar populations based on their color, thus their collective kinematic properties, I grouped the main sequence stars into six color groups on the H-R diagram based on color according to the criteria of Li et al. (2019). The rotational kinematics properties and the corresponding Oort

Consider to
change this
part to desci-
Gaia DR2, an
briefly mention
the new eDR3

not relevant
to the Oort
constant estima-
in the later
section?
You may put
these in the
Appendix.

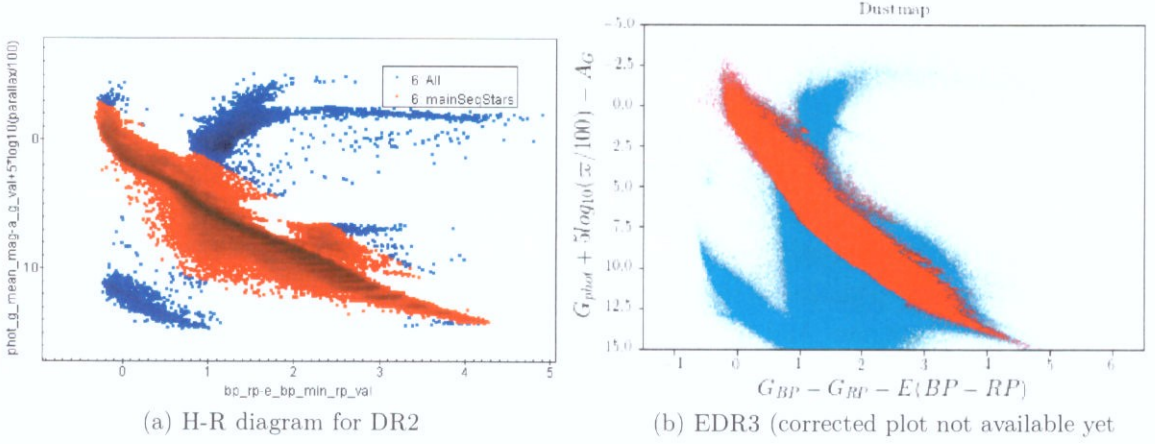


Figure 4: the H-R diagram and Main sequence star samples in DR2 and EDR3 after parallax, extinction and color excess correction.

constants for color group are analyzed individually. Table1 shows the number of stars in each stellar group, as well as the corresponding numbers in DR2.

$BP_RP - e_{bp}_{min}_{rp}_{val}$	< 0.8	$0.8 - < 1.2$	$1.2 - 1.6$	$1.6 - < 2.0$	$2.0 - 2.4$	≥ 2.4
DR2	978428	1591020	1284402	1086626	865742	351820
EDR3	649939	792940	1304201	2173292	347488	9356

Table 1: Number of main sequence stars fall into each color group for DR2 and EDR3. (will update these counts)

The proper motions and radial velocity entries in Gaia are measured in the equatorial coordinates system (ICRS), i.e. right ascension (α) and declination (δ) proper motions, μ_α and μ_δ . I used the SkyCoord class in *astropy* (Astropy Collaboration et al. 2018) to transform proper motions and available radial velocity from ICRS to the Galactic coordinate. The units of proper motion are also converted from mas yr⁻¹ to km s⁻¹ kpc⁻¹ by multiplying by a factor of 4.74047.

2.3. Deriving the Oort constants from Gaia DR2 data

I am planning to add a section here to clarify how I actually derive fit the Oort constants from the observational data:

- For each stellar group, we use the following process to derive the corresponding Oort constants from μ_l , μ_b and v_{los} :
- Using peculiar motion $(u_0, v_0, w_0) = (11.1, 12.24, 7.25)$ km/s (Schönrich, 2012) to find $\Delta\mu_l$, Δv_{los} and $\Delta\mu_b$.

- I will take their binned medians to show the longitudinal profile of each quantity. This is to see if I should include μ_b and v_{los} in fitting the Oort constants by MLW estimation.
- Fit all individual data points to the equations of $\Delta\mu_l$ (Δv_{los} and $\Delta\mu_b$ if from the step above the binned medians' dependency on l is fine).
- use MCMC in the next subsection to approximate the uncertainties in the derived Oort constants.

2.4. *Estimating the parameters and their corresponding uncertainties:
Monte-Carlo-Markov-Chain*

The parameters in the model of Eq 11, 12 and 13 consist of the four Oort constants and three peculiar velocity components. For such high-dimensional parameter space, I used the Monte Carlo Markov Chain (MCMC) method to determine the value and uncertainty of each parameter. The MCMC method combines our prior knowledge about the model and evidence from the data to obtain a posterior distribution of the model parameter θ , in this case, $\theta(A, B, C, K, u0, v0, w0)$. When fitting Gaia observational data in MCMC, the proper motions in longitude and latitude direction are considered together, but radial velocity is separated because this data is incomplete. The logarithmic likelihood function used is defined as:

$$\ln \mathcal{L}_\infty = - \sum_i \left(\frac{(med(\mu_l)_i - y_1)^2}{\sigma_{med(\mu_l)}^2 + error_{med(\mu_l)}^2} - \ln \frac{2\pi}{\sigma_{med(\mu_l)}^2 + error_{med(\mu_l)}^2} \right. \\ \left. - \frac{(med(\mu_b)_i - y_2)^2}{\sigma_{med(\mu_b)}^2 + error_{med(\mu_b)}^2} - \ln \frac{2\pi}{\sigma_{med(\mu_b)}^2 + error_{med(\mu_b)}^2} \right) \quad (14)$$

where $\sigma_{med(\mu_l)}$ and $\sigma_{med(\mu_b)}$ are the Gaussian scatter for the distribution of binned medians, $error_{med(\mu_l)}^2$ and $error_{med(\mu_b)}^2$ are the standard deviations within each bin, and y_1 and y_2 are given by Eq 12 and 13.

The prior distribution of θ is defined as following:

$$P(\theta) = \begin{cases} 0 & \text{if } 10 < A < 20, -15 < B < -5, -5 < C < 5, \text{ and } -5 < K < 5 \\ -\infty & \text{if } A, B, C \text{ and } K \text{ are not within the range above} \end{cases} \quad (15)$$

And the overall logarithmic posterior probability is:

$$LnP(\theta|y) = \begin{cases} lnL & \text{if } P(\theta) = 0 \\ 0 & \text{if } P(\theta) = -\infty \end{cases} \quad (16)$$

I employed the *emcee* (Foreman-Mackey et al. 2013) python package and posterior probability Eq 16 to sample and update Markov Chains in MCMC.

2.5. Test particle simulation

To know what behaviors are expected from the theoretical Oort constants model, and thus understand how the actual MW deviates from the theoretical model, we constructed a toy model simulation, treating stars as test particles in a fixed MW potential and assuming all the model constraints of the Oort constants and the Sun stays on a circular orbit. I sampled 20,000 of test particles from *galpy*'s quasi-isothermal distribution function to represent a thin 3D Milky Way galactic disk. The distance from the Sun to the Galactic center and the circular velocity at the solar radius are set to $R_0 = 8$ kpc and $v_0 = 220$ km/s respectively. The horizontal scale of the disc is 0.4 kpc, and the radial velocity dispersion is chosen as 10km/s. This distribution function provides planar and vertical profiles of the thin disc with analytic function dependent on the action integrals in an integrable, axisymmetric Hamiltonian (Binney 2010). The potential in the Hamiltonian is specified by MWPotential2014 (Bovy 2015).

MWPotential2014 serves as a simple and accurate model for the MW potential from fitting to a large variety of dynamical data. This potential model consists of a bulge potential with a power law exponent of 1.8 and a cut-off radius of 1.9kpc (PowerSphericalPotentialwCutoff), a disk potential specified by MiyamotoNagaiPotential, and a dark-matter halo described by an NFWPotential (Bovy 2015). Fig 5 shows the spatial distribution of test particles sampled from the quasi-isothermal distribution function.

Besides, because we set the peculiar motion of the Sun to 0, the coordinate and velocity of LSR and the Sun are equivalent. All particles undergo 10Gyr of orbit integration under the potential specified by MWPotential2014 to reach equilibrium. The positions and velocities after 10Gyr are then used to calculate μ_l and μ_b , as well as v_{los} . Similar to the procedure of analyzing Gaia data, I binned the simulation data and used the binned medians to fit the three equations in Eq 11, 12 and 13, except u_0 , v_0 , and w_0 are set to 0. The log likelihood for MCMC is defined as:

$$\ln\mathcal{L}_2 = \ln\mathcal{L}_1 - \sum_i \left(\frac{(med(v_{los})_i - y_3)_i^2}{\sigma_{med(v_{los})}^2 + error_{med(v_{los})}^2} - \ln \frac{2\pi}{\sigma_{med(v_{los})}^2 + error_{med(v_{los})}^2} \right) \quad (17)$$

where $\ln\mathcal{L}_1$ is from Eq 14, $\sigma_{med(v_{los})}$ is the Gaussian scatter for the distribution of binned medians of v_{los} , $error_{med(v_{los})}$ is the standard deviations within each bin of v_{los} , and y_3 is given by Eq 11.

3. RESULTS

3.1. Simulation: The effect of sampling criteria on μ_l , v_{los} , μ_b

From the simulation with 500,000 stars (test particles) described in above (Section 2.5), we examined the effect of different sampling criteria on the resulting proper motions (μ_l and μ_b) and the line-of-sight velocity (v_{los}) dependency on l . Fig 5a

displays the distribution of all the particles in 16 kpc from the GC and ± 4 kpc in the vertical direction. This disc looks thicker despite the scale height in the quasi-isothermal distribution function (Section 2.5) was set to 0.4 kpc because the tail of exponential distribution is evident when sample size is large. Out of the 500,000 particles, most reside on the other side of the Sun, far away from the Sun. In Fig 5b, we showed those stars within $d = 4$ kpc from the Sun. We replicated the Sun's position at another four symmetric three positions (0, 8kpc, 0), (-8kpc, 0, 0) and (0, -8kpc, 0) in the Cartesian form of the Galactocentric coordinate. This increases the number of stars nearby the Sun(s) so and gave us more available simulation results to analyze and derive the Oort constants.

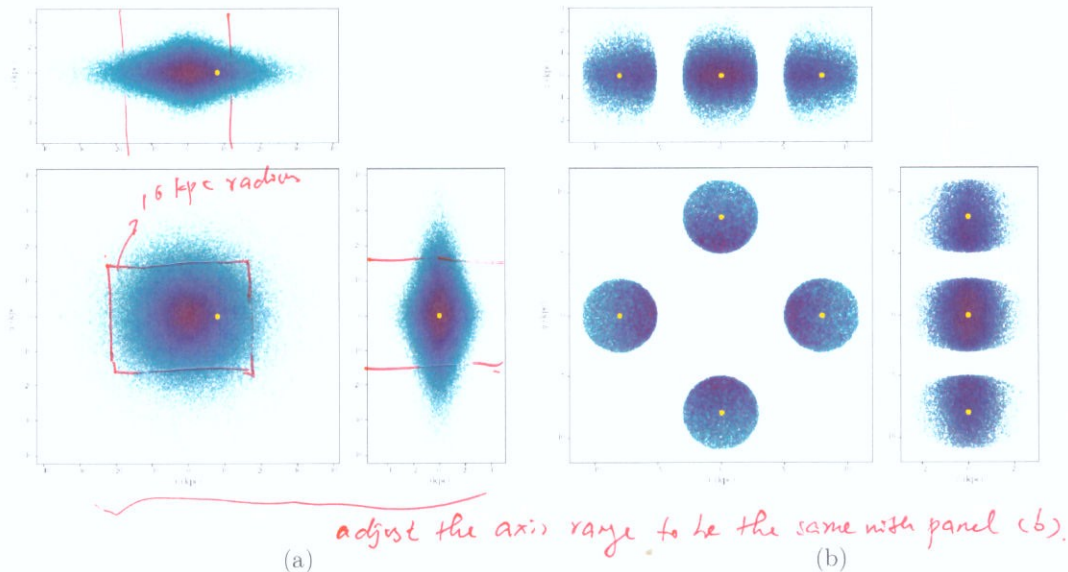


Figure 5: (a) The distribution of the 500,000 test particles (stars) sampled from quasi-isothermal distribution function for the Milky Way. (b) The distribution of simulated stars within $d = 4$ kpc from the Sun, where we replicated the Sun at four different positions to increase effective samples near the Sun. Darker color correspond to higher density. *symmetric* *the sizes of*

3.1.1. μ_l and v_{los}

In Fig 6, we present the result of μ_l vs l under three sample filtering criteria on the galactic distance d for stars that approximately lie on the mid-plane ($|b| < 20^\circ$). Proper motions after correcting the contribution in latitudinal direction ($\cos b$) are mostly negative across $l = 0^\circ$ to 360° , indicating that stars move in the decreasing l direction. Fig 6 also shows μ_l has slightly positive value at $l = 0^\circ, 180^\circ$, and 360° . *that*

* You should make all the figures to have the same size. It is ~~wrong~~ that one panel is larger than the other.

16

relatively
is most negative and has larger variation among stars with the same l value at $l = 90^\circ$ and 270° compared to the stars at $l = 0^\circ, 180^\circ$, or 360° . ~~the~~

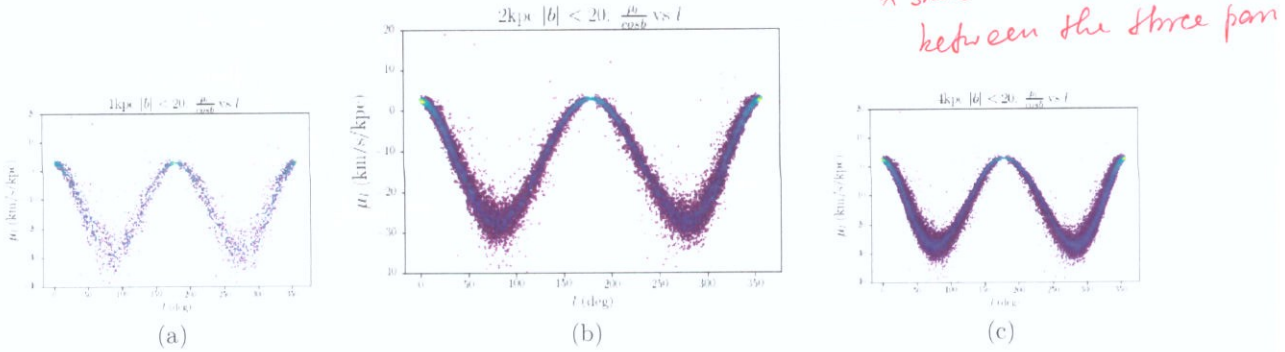


Figure 6: The distribution of $\mu_l / \cos b$ over l for stars with $|b| \leq 20$ and , (a) $d \leq 1\text{kpc}$, (b) $d \leq 2\text{kpc}$, and (c) $d \leq 4\text{kpc}$

In Fig 21a, we see for stars with $d < 2\text{kpc}$ and $|b| < 20$, v_{los} after divided by d traces a single double sinusoidal function as expected from Eq11. v_{los} is 0 at $l = 0^\circ, 90^\circ, 180^\circ, 270^\circ$. Positive v_{los} between $l = 0^\circ$ to 90° and $l = 180^\circ$ and 270° suggests stars move away from the Sun in the line of sight direction in these two l intervals. And stars approach the Sun in the line of sight direction between $l = 90^\circ$ and $180^\circ, 270^\circ$ and 360° . We show the comparison of v_{los}/d vs l if we keep $|b| < 20^\circ$ but constrain to stars to within 1kpc in Fig 7a and within 4kpc in 7c.

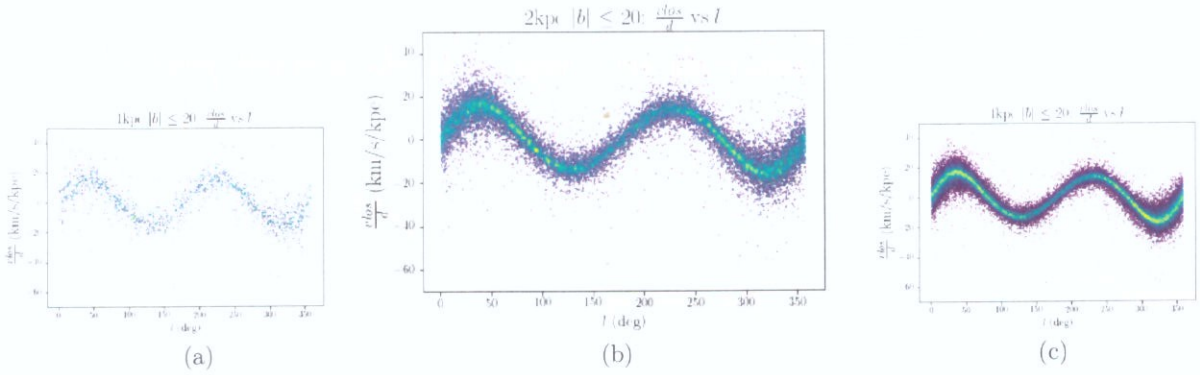


Figure 7: The distribution of v_{los}/d over l for stars with $|b| \leq 20$ and (a) $d \leq 1\text{kpc}$, (a) $d \leq 2\text{kpc}$, and (c) $d \leq 4\text{kpc}$

In Fig 8, we use a 2D velocity vector analysis of stars nearby the Sun at different ~~longitude~~ to illustrate the expected variation of μ_l and v_{los} . We assume these stars are all in circular orbits with radius R_{star} around the GC. At $l = 0^\circ$ and 180° , v_ϕ is in the line of LSR, and v_ϕ is perpendicular to the line of sight. As a result, $v_{los} = 0$ and

$v_l = v_\phi - v_{\phi\odot}$. According to the rotation velocity curve in (Fig 1), the radial profile of v_ϕ is flat while slightly declining at $R = R_\odot$. As a result, the star moves in the direction of increasing l , giving μ_l a small positive value at $l = 0^\circ$ in the inner side of the MW disk. At $l=180$, because v_ϕ is smaller than $v_{\phi\odot}$, the star lags behind the Sun, moving in the direction of increasing l , thus μ_l is expected to be positive (Fig 8b).

At $l = 90^\circ$ and 270° , stars are approximately in the same circular orbits as the Sun. They are essentially moving at the same speed as the Sun along the line of sight, thus $v_{los} = 0^\circ$. However, to examine their proper motion, we need to zoom in closer to show that v_{phi} varies slightly in their direction. And Fig 14 shows the perpendicular component v_l points in the decreasing l direction at both $l = 90^\circ$ and 270° . (which will be discussed later in section 3.1.4)

At $l = 45^\circ, 225^\circ, 135^\circ$ and 315° , the orange vectors in Fig 8a and 8b indicate the relative velocity in the line-of-sight and tangential l direction after comparing to the velocity of the Sun in each direction respectively. We show that at $l = 45^\circ$, $v_{los} > 0$ and $v_l < 0$; $l = 45^\circ$, $v_{los} < 0$ and $v_l < 0$; $l = 135^\circ$, $v_{los} > 0$ and $v_l < 0$; $l = 225^\circ$, $v_{los} > 0$ and $v_l < 0$; $l = 315^\circ$, $v_{los} > 0$ and $v_l < 0$.

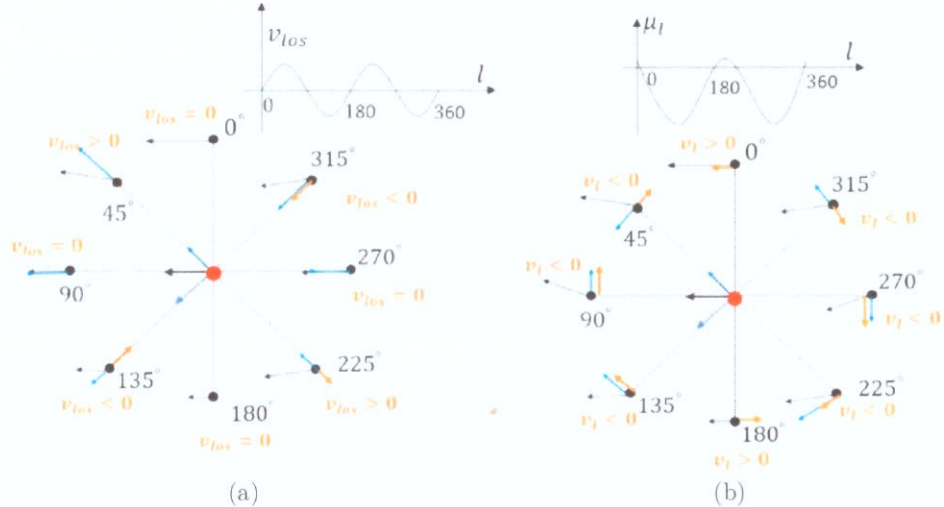


Figure 8: The variation in the radial velocity and transverse velocity among different Galactic longitude due to differential rotation of the Milky Way. The black arrows represent the velocity vector of v_ϕ . The blue vectors represent the components in the line of sight direction (Fig 8a) and the longitudinal direction (Fig 8b). The orange arrows are the relative velocity vectors in the two directions after taking the circular motion of the Sun into account.

3.1.2. The effect of the distance selection, d , on the longitudinal profile of μ_l and v_{los}

In Fig 6 and Fig 7, the number of samples selected drops from 51196 to 16741 and to 2310 as the galactic distance cut-off decreases from 4kpc, to 2kpc, and to 1kpc. While the dispersion of $\mu_l / \cos b$ and v_{los}/d are unaffected by the distance cut-off chosen in

Fig. 6 and Fig. 7
or

Figs. 6 and 7

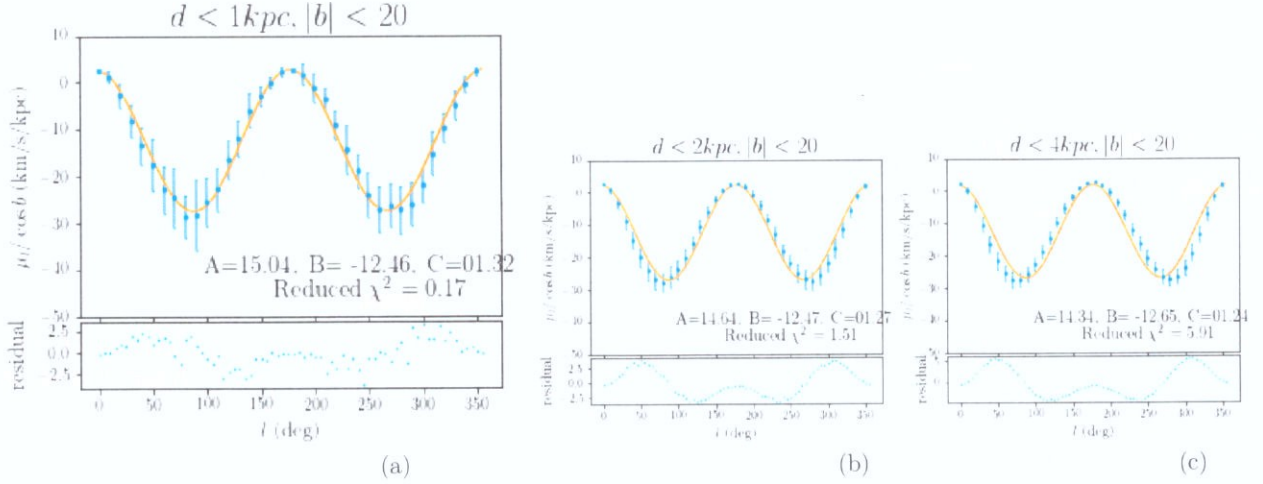


Figure 9: The function of binned median $\mu_l / \cos b$ over l for stars with $|b| \leq 20^\circ$ and (a) $d \leq 1\text{kpc}$, (b) $d \leq 2\text{kpc}$, and (c) $d \leq 4\text{kpc}$. The orange continuous curves come from fitting the binned median data to Eq 12 with maximum likelihood approximation. Only 36 out of 72 binned medians are plotted.

although the general trend is similar
→ to the dotted sinusoidal curves,

Fig. 6, the binned median values reveal some differences. In Fig 9, all the scatter data of Fig 6 are grouped into bins with a width of $l = 5^\circ$, and the median of μ_l in each bin is plotted against l . The error bars are the standard deviations of the corresponding bins. For simulated stars within 4kpc, there are significant deviations from the double cosine function (Fig 9c). This result suggests that 4kpc is too large for the first-order Taylor expansion around the Sun in Eq 6. The stars within 2kpc yield a reduced χ^2 closest to 1. However, including higher-order terms, such as $\sin(3l)$, $\cos(3l)$, etc would fit these simulated data points more accurately. (Is this due to using a larger region for Taylor expansion or physical reason? Need to expand here) The proper motions of stars within 1kpc from the sun trace the double sinusoidal function best compared to 2kpc and 4kpc, and the residuals are also smallest for this group. However, this galactic distance cut-off only yielded 2310 out of 500,000 that meet this filtering criteria. The standard deviation within each bin is larger because a smaller sample size is more subjective to the difference between individual values and the medians.

Similarly, the binned v_{los} median of stars within $d < 1\text{kpc}$ and $|b| < 20^\circ$ give v_{los}/d vs l closest to the function in Eq 11 compared to the stars within 4kpc and 2kpc. The reduced χ^2 values calculated for all the fitting above do not give informative measurements on the goodness of the fit. Reduced χ^2 being much larger than 1 suggests errors are underestimated, and overestimated for Reduced χ^2 being much smaller than 1. However for our simulated data, the errors come from standard deviation within each bin. Instead, we look at the range and distribution in the residual vs l profile to decide if the fit is satisfactory. For both $\mu_l / \cos b$ and v_{los}/d ,

No need to mention this
It is expected as you omit the higher orders in the Taylor expansion

the residual profiles for $d < 1$ kpc have the smallest ranges. Moreover, for the fittings of $d < 2$ kpc or $d < 4$ kpc samples, the residual distribution is not uniform above or below 0 but exhibits a clear dependency on l , while when $d < 1$ kpc, residual ~~is~~ are distributed randomly above and below 0. The dependency of residuals on l seems worthy of further investigation in future work, as it may hint to additional velocity structures.

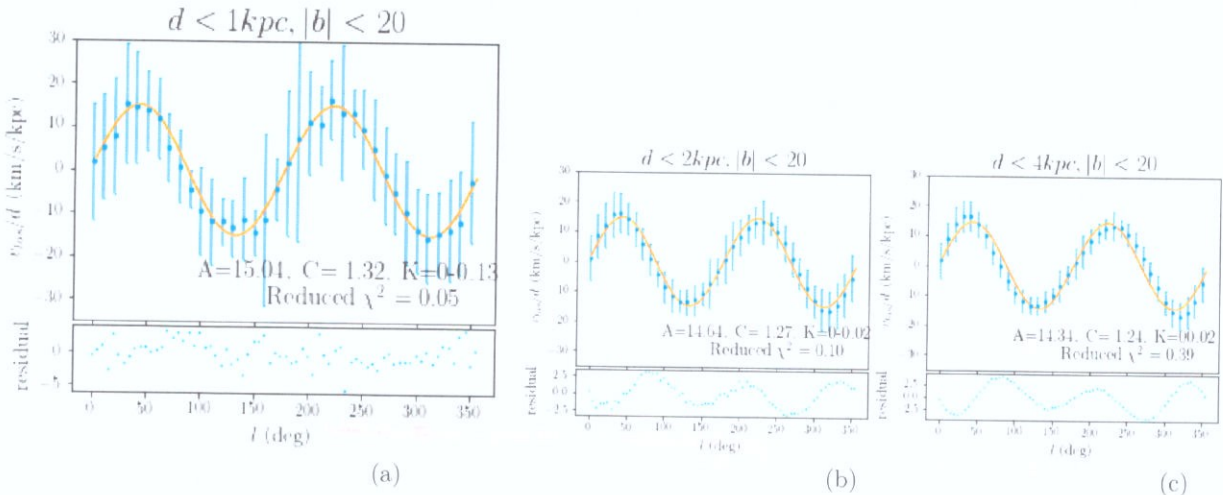


Figure 10: The function of binned median v_{los}/d over l for stars with $|b| \leq 20^\circ$ and (a) $d \leq 1\text{kpc}$, (b) $d \leq 2\text{kpc}$, and (c) $d \leq 4\text{kpc}$. The orange continuous curves come from fitting the binned median data to Eq 11 with maximum likelihood approximation. Only 36 out of 72 binned medians are plotted.

3.1.3. The effect of Galactic latitude ~~selection~~^{range} b on the longitudinal profiles of μ_l and v_{los}

In Fig 11, we compared binned μ_l median vs l of stars at $d < 2\text{kpc}$ from the Sun but at different latitude ranges, $|b| < 20^\circ$, $30^\circ < |b| < 50^\circ$ and $60^\circ < |b| < 80^\circ$. The scatter in the μ_l around the central double sinusoidal line increases for higher latitude regions as suggested by the error bars on the binned median data. When $|b| \leq 20^\circ$, stars are considered close to the MW mid-plane, thus are most suitable to fit the model in Eq 12. For $30^\circ \leq |b| \leq 50^\circ$, the scattered data deviate from the double cosine function considerably. And for $60^\circ \leq |b| \leq 80^\circ$, not only the spread in the scattered data is the largest, the binned medians deviate from the fitted double cosine function more significantly according to the residual vs l panel in Fig 11.

Likewise, in Fig 12, the spread in the v_{los}/d of the stars within 2kpc from the Sun but at a higher latitude b is larger. Comparing the residual profiles in the lower panels, we see the range of residuals is the smallest for the group closest to the MW mid-plane. This suggests ~~that~~ the deviation of binned v_{los}/d median from the predicted double sine function is smallest for stars at $|b| < 20^\circ$ and largest at $60^\circ < |b| < 80^\circ$. With a larger latitude limit, we move away from the Milky Way (~~MW~~) disk, and

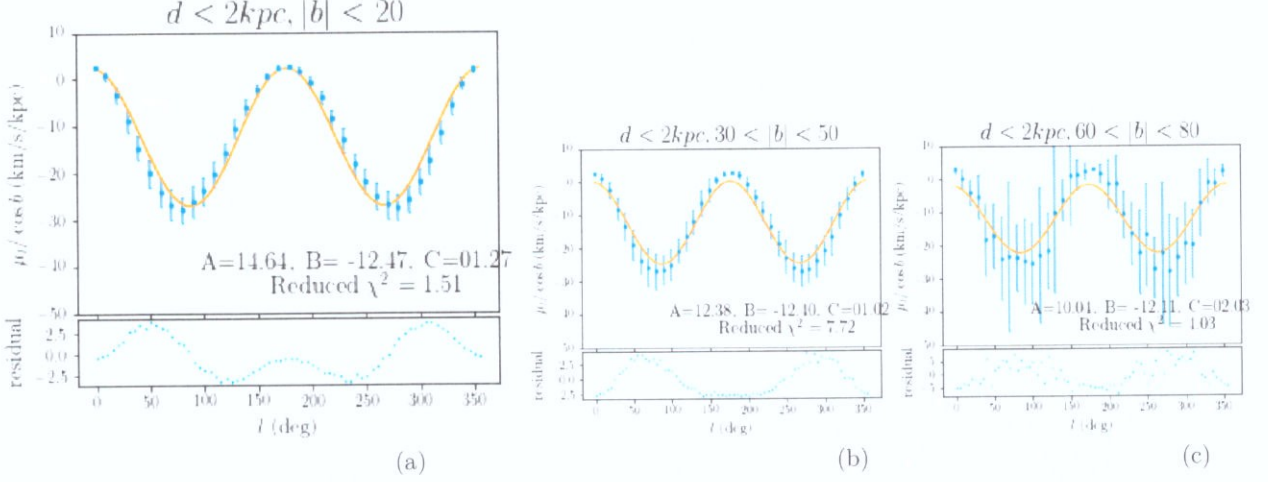


Figure 11: The function of binned median $\mu_l/\cos b$ over l for stars with $d < 2\text{kpc}$ and (a) $|b| \leq 20^\circ$, (b) $30^\circ < |b| < 50^\circ$, and (c) $60^\circ < |b| < 80^\circ$.

the orbits get less circular. MW potential gradient in the z-direction is large enough to add significant vertical perturbations at high latitude region, tilting the circular orbits ~~that would otherwise stay on a plane parallel to the MW mid-plane~~. Therefore, we expect that the deviation is significant for stars at $60^\circ < |b| < 80^\circ$ in the Solar vicinity.

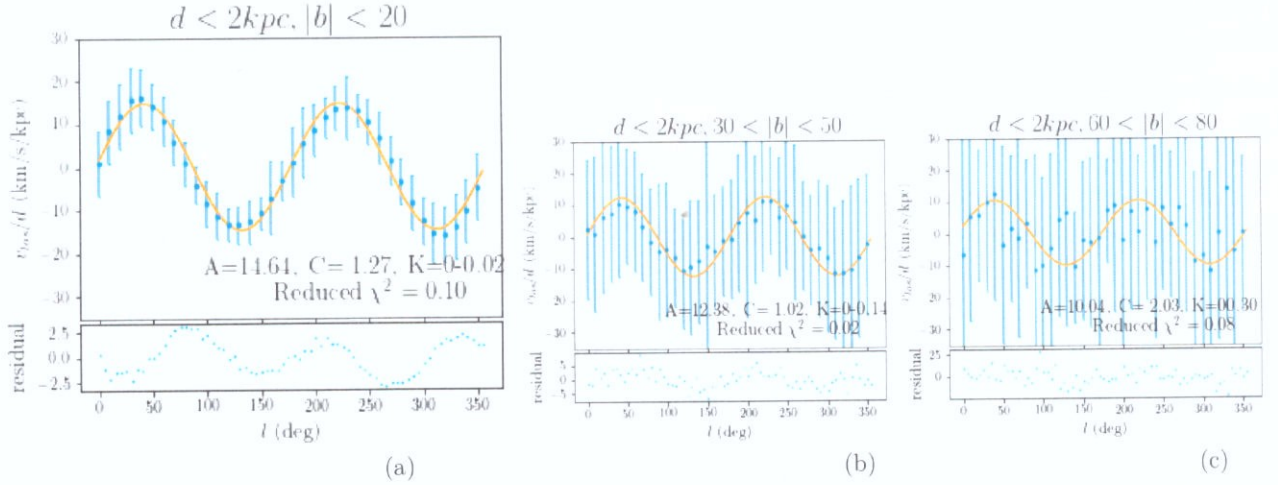


Figure 12: The function of binned median v_{los}/d over l for stars with $d < 2\text{kpc}$ and (a) $|b| \leq 20^\circ$, (b) $30^\circ < |b| < 50^\circ$, and (c) $60^\circ < |b| < 80^\circ$.

3.1.4. Longitudinal profiles of μ_b

For proper motion in the latitude direction, μ_b , we expect to see more nonzero value at the region always from the Galactic plane with ~~larger and middle range~~ $|b|$
 Far away ~~middle range~~ *relatively large*

because of the product $\sin b \cos b$ in Eq 13. In Fig 13, contrast to μ_l and v_{los} discussed above, the value of $\mu_b / \cos b \sin b$ of stars with $d < 2\text{kpc}$ and $30^\circ < |b| < 50^\circ$ are much more dispersed. In Fig 15, taking binned medians gives the double sinusoidal curve expected from Eq 13. The binned standard deviations for these binned μ_b medians range from 50-100 km/s/kpc, much larger than the variation of the binned medians across l , ($\pm 25\text{km/s/kpc}$). Thus, error bars are not plotted in Fig 15 to better show the dependency of binned $\mu_b / \cos b \sin b$ medians on l . At $l = 0^\circ, 90^\circ, 180^\circ, 270^\circ$, $\mu_b = 0$. Stars are descending from the perspective of LSR from $l = 0$ to 90° and from 180 to 270° while ascending from $l = 90^\circ$ to 180° and from 270° to 360° .

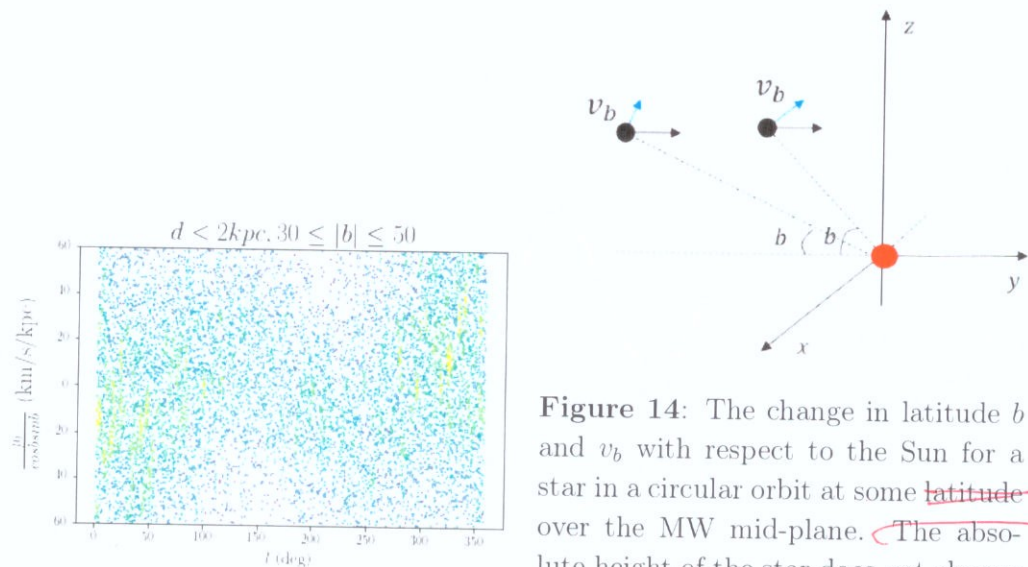


Figure 13: Longitudinal profiles of $\mu_b / \cos b \sin b$ for stars with $d < 2\text{kpc}$, $30^\circ < |b| < 50^\circ$

Because the derivation of Oort constants assumes stars are close to the MW mid-plane, the discussions on μ_l and v_{los} are more prevalent than the motion approaching or leaving the MW mid-plane. In fact, μ_b , the proper motion in the latitudinal direction is also a kinematic tracer of the MW differential rotation. In Fig 14, let's look at a star at some vertical distance from the MW mid-plane and on a ~~circular~~ hypothetical orbit with a constant v_ϕ and $v_z = 0$.¹ As this star rotates around the GC at a different v_ϕ than the Sun, its relative position with respect to the Sun changes, so it appears to approach or move away from the Sun while maintaining its absolute height. The angle between the line-of-sight and the horizontal plane parallel to the Milky Way mid plane, which is just the Galactic latitude b , result a $\sin b$ velocity component in

Figure 14: The change in latitude b and v_b with respect to the Sun for a star in a circular orbit at some ~~latitude~~-vertical height over the MW mid-plane. The absolute height of the star does not change because $v_z = 0$, but its Galactic latitude changes as it approaches or moves away from the Sun.

~~hypothetical~~

¹ Such an orbital configuration is not valid. We only use it for the purpose of demonstrating the connection between μ_b and differential v_ϕ around the Milky Way center.

the Galactic latitude b direction perpendicular to the line-of-sight, v_b . As illustrated in Fig 14, this b angle varies when the star moves closer or away from the sun, so does v_b . Therefore, $\mu_b = \frac{v_b}{d}$ is also a tracer for the stellar in-plane motion. Its dependency on l can be used to derive Oort constants and study the differential rotation of the Milky Way. This component, v_b , is larger for stars with higher b because of the $\sin b$ component. Thus, in our simulation, we look at μ_b of stars with mid range b values. However, for stars with very high $|b|$, that is away from the disc in the vertical direction, their orbits are rather non-circular due to the potential perturbation in the vertical direction. These stars tend to have larger vertical velocities, which can give a more dominant contribution to μ_b than the effect coming from differential rotation discussed above.

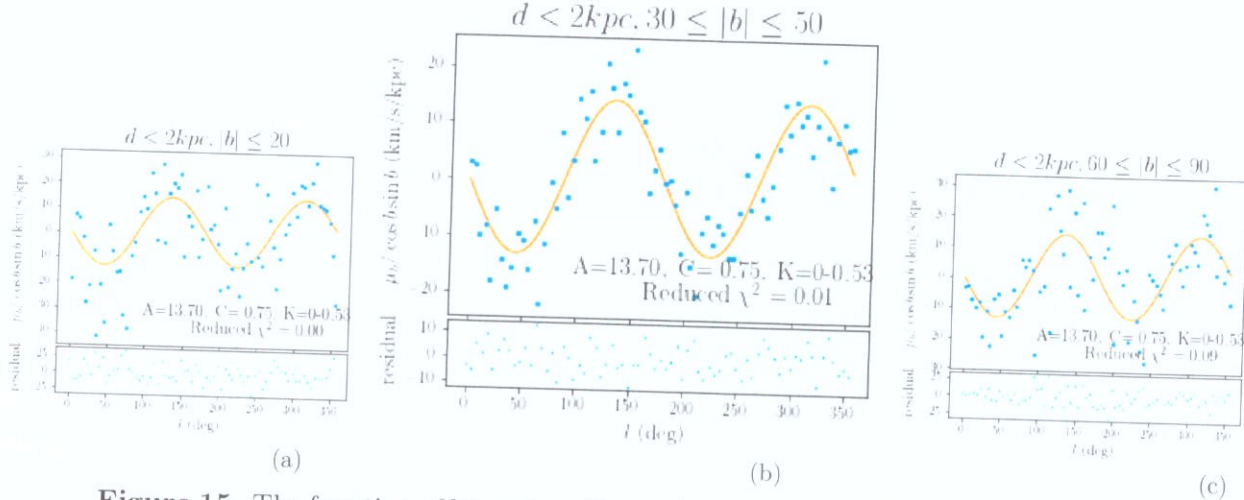


Figure 15: The function of binned median $\mu_b / \cos b \sin b$ over l for stars with $d < 2\text{kpc}$ and ,(b) $|b| \leq 20^\circ$,(b) $30^\circ \leq |b| \leq 50^\circ$, and (c) $60^\circ \leq |b| \leq 90^\circ$

In Fig 15, compared to the stars closer to the MW disk ($|b| < 20^\circ$) or those that are much farther away from the MW disk ($|b| > 60^\circ$), stars with $|b|$ between 30° and 50° yield the most noticeable double sinusoidal variation with l . In the residuals profiles, the residual for the group with $30^\circ < |b| < 50^\circ$ distribute randomly over the smallest range compared to the other two groups. This suggests the group with $30^\circ < |b| < 50^\circ$ gives the most satisfactory fit to the model predicted by Eq 13.

On the other hand, in Fig 16, for larger spatial coverage, $d < 4\text{kpc}$, binned median of $\mu_b / \cos b \sin b$ shows a more evident double sinusoidal function than stars within 2kpc and 1kpc. The residual vs l panels suggests that the dispersion about the medians is the least when all the samples in a larger region around the Sun are included. This is likely because for a larger sample size, the binned medians are less subjective to any extreme individual values. However, the trade-off for including more samples is applying the first-order Taylor expansion in a much larger region than Sun vicinity.

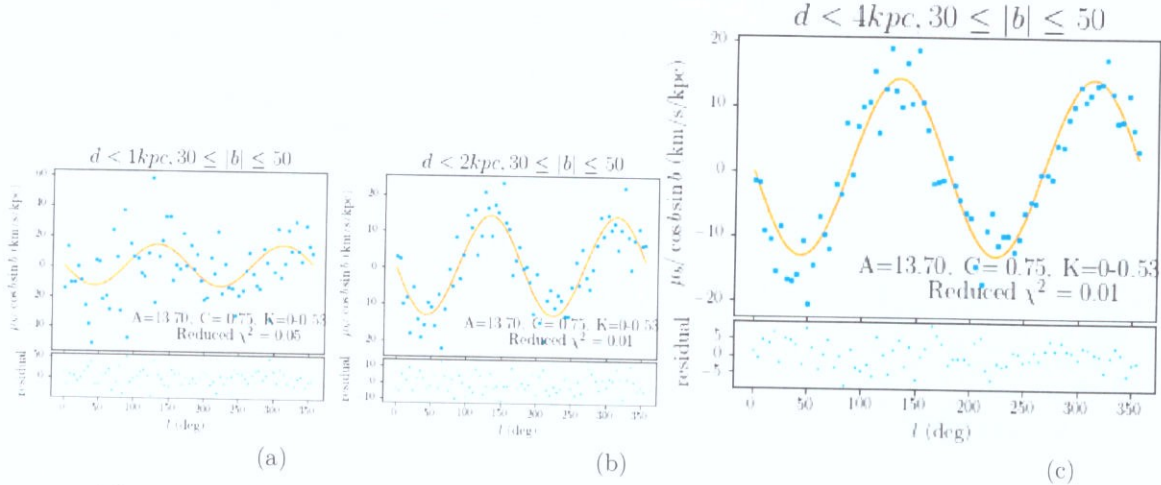


Figure 16: The function of binned median $\mu_b / \cos b \sin b$ over l for stars with $30^\circ \leq |b| \leq 50^\circ$ and ,(a) $d \leq 1\text{kpc}$,(b) $d \leq 2\text{kpc}$, and (c) $d \leq 4\text{kpc}$.

In Fig. 16c, the first trough at $l = 45^\circ$ is lower than the second one at $l = 225^\circ$. This suggests that the double sinusoidal function from the first-order Taylor expansion possibly under-approximate higher order dependency proportional to $\sin(3l)$, $\sin(4l)$ and so on.

3.2. The effect of radial and vertical velocity values on μ_l , v_{los} , μ_b

In Appendix 22, we include the longitudinal profiles $\mu_l / \cos b$, v_{los}/d and binned median of $\mu_b / \cos b \sin b$ under different constraints on radial velocity v_r and vertical velocity v_z : 1) no constraints on v_r and v_z ; 2) setting $v_r = 0$; and 3) setting $v_z = 0$. The result shows the spread in μ_l is due to the variation of v_r . Both v_r and v_z make contributions to the scattering in v_{los}/d . When v_r is set to 0, the scattering around the central double sine curve is smaller as the brighter color indicates a higher density. Meanwhile, the contribution to the scattering in v_{los}/d by v_z is more significant. The difference of the binned median of μ_b under three velocity profiles shows the deviations from the double sine function described by the Oort constants is attributed to the non-zero vertical velocity stars, agreeing well with the discussion in section 3.1.4. *consistent*

The difference is much smaller than the error. It may not be meaningful to discuss this.

* You can consider to provide Fig. 22 from the Appendix + here in the main text.

3.3. Gaia DR2 observational data

3.3.1. Gaia DR2: using the filtering criteria from literature

We now present results using Gaia DR2 data described in Section 2. In Fig 17, we show the $\Delta\mu_l$ as a function of l in the region within $d < 500\text{pc}$ and $|b| < 20^\circ$ for stellar populations with $G_{BP} - G_{RP} - E(BP_RP) < 0.8$, $0.8 \sim 1, 2$, $1.2 \sim 1.6$, $1.6 \sim 2.0$, $2.0 \sim 2.4$ and ≥ 2.4 . *The plots are not quite correct.* At least for the first three stellar population based on color, the binned medians of $\Delta\mu_l$ vs l fits Eq12. The deviation from the double cosine function is larger for redder stellar populations

$\Delta\mu_l$.

as we move across panels (a) to (d) in Fig 17. This is consistent with the fact that redder stars are kinematically ~~older~~ ^{hotter} and reside in ~~hotter~~ less circular orbits. We also notice that there is a population of stars concentrated at $l = 280^\circ$ and μ_l around 20 km/s/kpc.

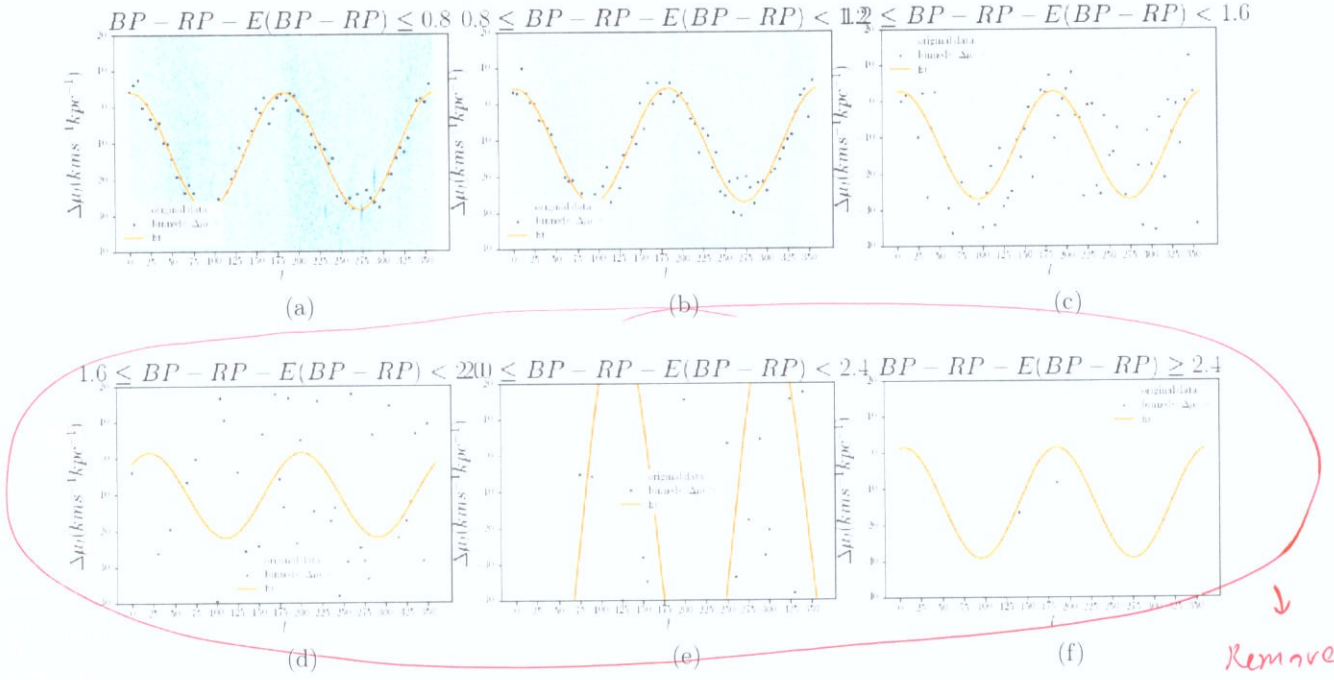


Figure 17: $\Delta\mu_l$ as a function of l for stars with $d < 500$ pc and $|b| < 20^\circ$ divided into groups with $G_{BP} - G_{RP} - E(BP - RP) < 0.8$, $0.8 \sim 1, 2$, $1.2 \sim 1, 6$, $1.6 \sim 2.0$, $2.0 \sim 2.4$ and ≥ 2.4 . I really don't have the time to check what went wrong with these plots and add error bars. Forgive me, will do all of them this week

Similar to μ_l , v_{los} for the two bluest stellar populations calculated from the radial velocity data in DR2 are also well described by the double sine function predicted by the Oort constants (Fig 18). Despite ~~that the~~ radial velocity data entry is not available for all the stars in DR2, the two bluest stellar populations in Fig 18 show ~~that~~ v_{los} can be used to derive the Oort constants. Table 2 shows the estimated peculiar motion (u_0, v_0, w_0) from fitting μ_l in Fig 17 by maximum likelihood estimation. v_{los} in Fig 18 is included into the log likelihood function for the three bluest stellar populations.

While the l dependencies of μ_l and v_{los} for the stars in DR2 are consistent with the equations of the Oort constants, μ_b for stars in the Solar vicinity and middle $|b|$ range do not follow the curve predicted by Eq 13 as nicely as μ_l and v_{los} do. Only for the bluest stellar population, $\delta\mu_b$ follows the double sinusoidal curve. This suggests that μ_b is a less ideal tracer for deriving the Oort constants.

$$\delta\mu_b$$

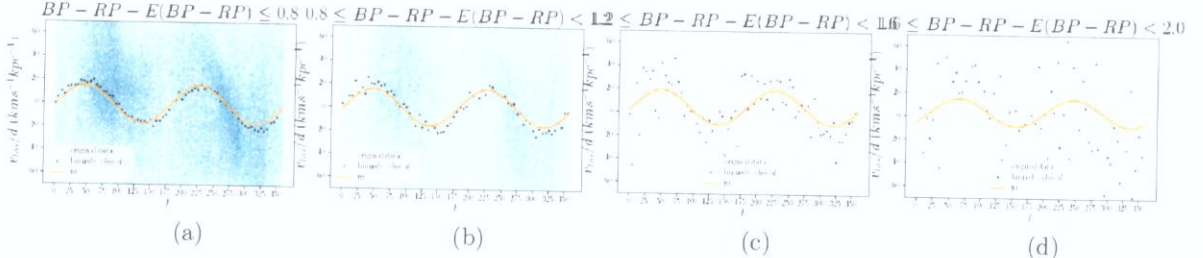


Figure 18: Δv_{los} as a function of l for stars with $d < 500 \text{pc}$ and $|b| < 20^\circ$ divided into groups with $G_{BP} - G_{RP} - E(BP - RP) < 0.8$, $0.8 \sim 1, 2$, $1.2 \sim 1.6$, and $1.6 \sim 2.0$.

	$u_0(\text{km s}^{-1})$	$v_0(\text{km s}^{-1})$	$w_0(\text{km s}^{-1})$
$G_{BP} - G_{RP} - E(BP - RP) < 0.8$	10.85	19.44	7.07
$0.8 \leq G_{BP} - G_{RP} - E(BP - RP) < 1.2$	11.10	21.19	3.43??
$1.2 \leq G_{BP} - G_{RP} - E(BP - RP) < 1.6$	10.95	21.32	-45.15 ???
$1.6 \leq G_{BP} - G_{RP} - E(BP - RP) < 2.0$			
$2.0 \leq G_{BP} - G_{RP} - E(BP - RP) < 2.4$			
$G_{BP} - G_{RP} - E(BP - RP) \geq 2.4$			

Table 2: The value of solar peculiar motion (u_0, v_0, w_0) from fitting μ_l and v_{los} in Fig 17 and Fig 18 if available.

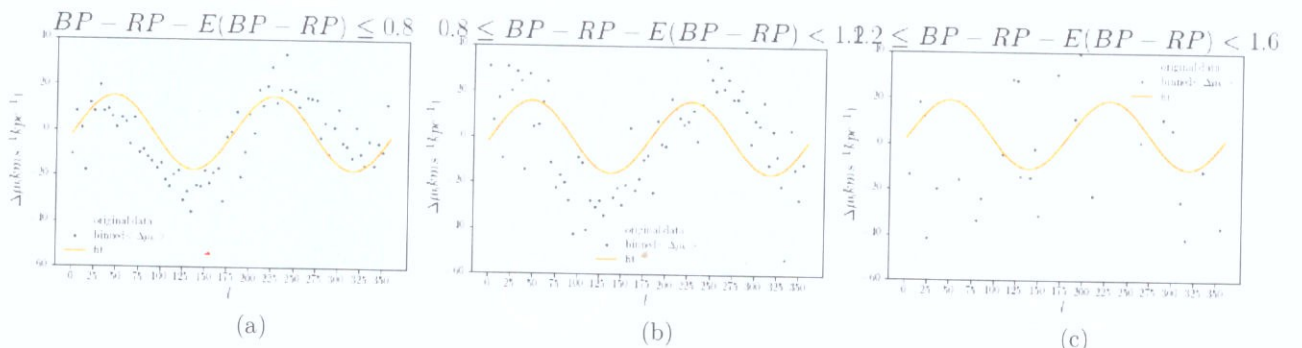


Figure 19: $\Delta \mu_b$ as a function of l for stars with $d < 500 \text{pc}$ and $40^\circ < |b| < 50^\circ$ divided into groups with $G_{BP} - G_{RP} - E(BP - RP) < 0.8$, $0.8 \sim 1, 2$, and $1.2 \sim 1.6$.

Table 3 lists the values of the Oort Constants and their uncertainties estimated from the results in Fig 17, 18 and 19 using MCMC (See Appendix. X for the MCMC corner plot).

3.3.2. Applying filtering criteria based on Simulation to Gaia DR2

No result yet.

3.4. EDR3

: Have not decided if we should apply similar analysis to EDR3.

Maybe just

This is important
You should put
the mcmc result
here!

$G_{BP} - G_{RP} - E(BP - RP)$	$A(\text{km/s/kpc})$	$B(\text{km/s/kpc})$	$C(\text{km/s/kpc})$	$K(\text{km/s/kpc})$
< 0.8	16.09	-12.39	-1.19	-1.33
≥ 0.8 and < 1.2	15.65	-11.54	-1.73	-0.36
≥ 1.2 and < 1.6	14.73	-12.31	-2.14	3.72
≥ 1.6 and < 2.0				
≥ 2.0 and < 2.4				
≥ 2.4				

Table 3: The values of the Oort Constants and their uncertainties estimated from the results in Fig 17, 18 and 19 using MCMC.

4. DISCUSSION

Based on the comparison of the longitudinal profiles of μ_l and v_{los} under different galactic distance and latitudinal restriction in the result section above, we chose $d < 2\text{kpc}$ and $|b| < 0$ as the sampling criteria in extracting the longitudinal profiles of $\mu_l/\cos b$ and v_{los}/d . With MCMC, we determined the best-fitting parameters and their uncertainty: $A = 14.63 \pm 0.28, B = -11.96 \pm 0.29, C = 1.25 \pm 0.23, K = 0.09 \pm 0.66$, in the unit of km/s/kpc. (See Appendix XX for the corner map of the MCMC approximation)

Meanwhile, Gaia DR2 data of the two bluest stellar population, $BP - RP - E(BP - RP) < 1.2$, in 500pc from the Sun and less than 20° in the latitudinal direction yields the following measurement on A, B, C and D (Li et al. ?)

$$A = 15.93 \pm e1, B = -12.06 \pm e2, C = -1.30 \pm e3, K = -1.13 \pm e4 \text{ km/s/kpc}, \quad (18)$$

and the derived solar motion about LSR is:

$$u_0 = 10.97, v_0 = 20.24, w_0 = 8.65 \text{ km/s}. \quad (19)$$

The measurements for A and B from simulation and our analysis on Gaia DR2 are in good agreement with those obtained in XX. The local gradient of the rotation curve is given by $\frac{dv_\phi}{dR} = -(A + B)$. According to our results from both simulation and Gaia DR2, $-(A + B)$ is negative. It indicates the circular velocity decreases in Solar vicinity, which is in agreement with the rotation curve in Fig 1.

Recall in the Introduction, we mentioned that the mean offset value K describes the divergence in the local velocity field. K from simulation is not significantly different from 0, confirming that Milky Way simulated from quasi-isothermal distribution is axisymmetric. On the other hand, the non-zero mean offset derived from Gaia DR2 shows the motions in our actual Milky Way is non-axisymmetric.

(Comments on the solar peculiar motion derived in Table 2.) Consistent with Li?

Our result with μ_b from simulation and Gaia DR2 do not agree with Li et al. 2019. Why? I don't know. For Gaia DR2 data, the comparison of the v_ϕ vs v_r phase plot between stars with $|b| < 20^\circ$ and $40^\circ < |b| < 50^\circ$ in Appendix Fig 23 shows that the radial velocities about the GC for the stars with $40^\circ < |b| < 50^\circ$ are distributed over

a larger non-zero range than the stars with $|b| < 20^\circ$. This suggests the stars we used to derive Oort constants from their proper motions in the latitudinal direction reside in less circular orbits. Because the assumption for Oort constants is circular orbital motion, more consideration is needed when using μ_b to derive the Oort constants. In Section 3.2, we showed that μ_b has strong double sinusoidal dependency on l as predicted by Eq 12 when the stars are in purely circular motions parallel to the MW mid-plane ($v_{\pm 0}$ and $v_z = 0$). ↙ float

5. CONCLUSION

→ suggesting the possible connection between rotation and the latitudinal proper motion.

End with real summary and future direction

ACKNOWLEDGMENTS

This work has made use of data from the European Space Agency (ESA) mission *Gaia* (<https://www.cosmos.esa.int/gaia>), processed by the *Gaia* Data Processing and Analysis Consortium (DPAC, <https://www.cosmos.esa.int/web/gaia/dpac/consortium>). Funding for the DPAC has been provided by national institutions, in particular the institutions participating in the *Gaia* Multilateral Agreement.

I would like to acknowledge the tremendous opportunity to do this work offered by Dr.Zhaoyu Li and Dr.Juntai Shen from Shanghai Jiaotong University, as well as Prof. Karen Masters, and their continuous supports throughout the project.

Software: Astropy (Astropy Collaboration et al. 2013, 2018), galpy (Bovy 2015), emcee (Foreman-Mackey et al. 2013).

REFERENCES

- Astropy Collaboration, Robitaille, T. P., Tollerud, E. J., et al. 2013, A&A, 558, A33, doi: [10.1051/0004-6361/201322068](https://doi.org/10.1051/0004-6361/201322068)
- Astropy Collaboration, Price-Whelan, A. M., SipHocz, B. M., et al. 2018, aj, 156, 123, doi: [10.3847/1538-3881/aabc4f](https://doi.org/10.3847/1538-3881/aabc4f)
- Binney, J. 2010, MNRAS, 401, 2318, doi: [10.1111/j.1365-2966.2009.15845.x](https://doi.org/10.1111/j.1365-2966.2009.15845.x)
- Binney, J., & Merrifield, M. 1998, Galactic Astronomy
- Bovy, J. 2015, ApJS, 216, 29, doi: [10.1088/0067-0049/216/2/29](https://doi.org/10.1088/0067-0049/216/2/29)
- . 2017, MNRAS, 468, L63, doi: [10.1093/mnrasl/slx027](https://doi.org/10.1093/mnrasl/slx027)
- Eilers, A.-C., Hogg, D. W., Rix, H.-W., & Ness, M. K. 2019, ApJ, 871, 120, doi: [10.3847/1538-4357/aaf648](https://doi.org/10.3847/1538-4357/aaf648)
- Feast, M., & Whitelock, P. 1997, MNRAS, 291, 683, doi: [10.1093/mnras/291.4.683](https://doi.org/10.1093/mnras/291.4.683)
- Foreman-Mackey, D., Hogg, D. W., Lang, D., & Goodman, J. 2013, PASP, 125, 306, doi: [10.1086/670067](https://doi.org/10.1086/670067)
- Gaia Collaboration, Brown, A. G. A., Vallenari, A., et al. 2020, arXiv e-prints, arXiv:2012.01533, <https://arxiv.org/abs/2012.01533>
- Gaia Collaboration, Prusti, T., de Bruijne, J. H. J., et al. 2016, A&A, 595, A1, doi: [10.1051/0004-6361/201629272](https://doi.org/10.1051/0004-6361/201629272)
- Gaia Collaboration, Brown, A. G. A., Vallenari, A., et al. 2018, A&A, 616, A1, doi: [10.1051/0004-6361/201833051](https://doi.org/10.1051/0004-6361/201833051)
- Green, G. 2018, The Journal of Open Source Software, 3, 695, doi: [10.21105/joss.00695](https://doi.org/10.21105/joss.00695)